Available online at www.sciencedirect.com
SCIENCE DIRECT®
International Journal of Heat and Mass Transfer 49 (2006) 2420–2436
International Journal of HEAT and MASS TRANSFER
www.elsevier.com/locate/ijhmt

Three-dimensional numerical simulation of non-condensables accumulation induced by steam condensation in a non-vented pipeline

Vladimir D. Stevanovic [a,*], Zoran V. Stosic [b], Uwe Stoll [b]

[a] University of Belgrade, Kraljice Marije 16, 11120 Belgrade 35, Serbia and Montenegro
[b] Framatome ANP GmbH, P.O. Box 3220, D-91050 Erlangen, Germany

Available online 19 April 2006

Abstract

A substantial increase of the concentration of non-condensable gases in the mixture with steam can occur in a non-vented pipeline due to the condensation. This phenomenon is investigated with the thermal-hydraulic and physicochemical code HELIO. The hydrogen and oxygen accumulation is simulated and analyzed for a real non-vented steam pipeline of the nuclear power plant. The results show the propagation of non-condensables concentration front, the temperature and velocity field of the steam–non-condensables mixture, and the velocity and thickness of the condensate that drains on the pipeline's inner walls. The gas mixture temperature is verified with measurements from a full size test facility. The presented modelling approach and numerical results are unique regarding the simultaneous solution of the heat and mass transfer in the system consisting of the steam–non-condensable gases mixture and the thin liquid film on the pipe's wall.

Keywords: Condensation; Hydrogen; Non-condensable; Accumulation; Numerical simulation; HELIO

1. Introduction

Certain amounts of hydrogen and oxygen are present in coolants of light water nuclear reactors during the normal operation. They are mainly produced by the radiolytic water decomposition [1]. The hydrogen and oxygen concentrations in non-vented steam pipelines could be further substantially increased due to the steam condensation. The condensed steam is drained, while the concentration of remaining non-condensable hydrogen and oxygen increases. The operational experience of nuclear power plants has shown that even an explosive mixture of hydrogen and oxygen could be reached. Recently, this phenomenon caused two incidents of hydrogen and oxygen explosion at auxiliary systems of the Boiling Water Reactor (BWR) plants, in November 2001 in the Hamaoka plant in Japan [2] and one month latter in the Brunsbuettel plant in Germany [3,4].

The hydrogen and oxygen accumulation within non-vented steam pipelines is driven by coupled thermal-hydraulic and diffusion transport phenomena, such as the steam condensation in the presence of non-condensables, the condensate drainage, the non-condensables absorption at the liquid film surface, and the non-condensables transport by diffusion in the gas mixture with steam and by gas mixture convection. The steam–non-condensables gas mixture convection is induced by the replenishment of the condensed steam volume with the inflowing fresh steam–non-condensables mixture, by the temperature and concentration induced buoyancy forces and by the gas mixture shear at the moving liquid film surface. After several days, weeks or even months (depending on the heat loss to the surrounding atmosphere, which determines the condensation rate) an explosive hydrogen–oxygen mixture could

* Corresponding author. Tel.: +381 11 3370 561; fax: +381 11 3370 364.
E-mail address: estevavl@eunet.yu (V.D. Stevanovic).

0017-9310/$ - see front matter © 2006 Elsevier Ltd. All rights reserved.
doi:10.1016/j.ijheatmasstransfer.2006.01.029

Nomenclature

A	area, m^2
a	interfacial area concentration, m^{-1}
c_p	specific heat, J kg^{-1} K^{-1}
D	diffusion coefficient, m^2 s^{-1}, pipe diameter, m
D_h	hydraulic diameter, m
f	friction coefficient
g	mass fraction, gravity, m s^{-2}
h	heat transfer coefficient, W m^{-2} K^{-1}, specific enthalpy, J kg^{-1}
k	thermal conductivity, W m^{-1} K^{-1}
M	molar mass, kg $kmol^{-1}$
n	indicator of straight pipe ($n = 1$) or elbow ($n = 2$) in Eqs. (2) and (4)
p	pressure, Pa
p_c	partial pressure of gas mixture component, Pa
q_A	heat flux, W m^{-2}
R	radius of the pipe curvature (Fig. 2), m
Re	Reynolds number
r	radial coordinate, m
T	temperature, K, °C
t	time, s
u, v, w	velocity components, m s^{-1}
V	volume, m^3
x	coordinate, m

Greek symbols

α	volume fraction
Γ_{con}	rate of condensation, kg m^{-3} s^{-1}
Γ_a	rate of absorption, kg m^{-3} s^{-1}
δ	liquid film thickness, m
θ	circumferential coordinate, rad
λ	latent heat of condensation, J kg^{-1}
μ	dynamic viscosity, kg m^{-1} s^{-1}
ρ	density, kg m^{-3}
σ	surface tension, N m^{-1}
τ	shear stress, N m^{-2}

Subscripts

atm	parameter of the surrounding atmosphere
c	non-condensable component of the gas mixture
CV	control volume
H_2	hydrogen
i	liquid film surface, gas mixture–liquid film interface
in	insulator
O_2	oxygen
w	wall
σ	related to surface tension
1	liquid film
2	gas mixture

Abbreviations

BWR	boiling water reactor
CMFD	computational multi-fluid dynamics
NPP	nuclear power plant
RHRS	residual heat removal system

be formed, providing a risk for eventual hydrogen explosion and destruction of components integrity. At the plant the presence of the radiolytic gases is monitored by a number of temperature measurements located at non-vented pipelines' segments, devices and vessels where the radiolytic gases accumulation is expected [3]. Namely, the increase of radiolytic gases concentration decreases the steam partial pressure and consequently decreases the saturation temperature and steam–radiolytic gases mixture temperature. Although a substantial experience with the mechanisms of radiolytic gases accumulation is gained in the past, there are still unresolved questions and uncertainties about the possibilities and dynamics of these processes [3].

After the incidents in the Hamaoka and Brunsbuettel plants corresponding investigations have been performed. The non-condensable radiolytic gases accumulation in the non-vented steam pipeline in the Residual Heat Removal System (RHRS) of the Hamaoka Nuclear Power Plant was investigated at the 1:1 scaled experimental test facility [2]. For safety reasons, hydrogen is replaced by helium as a light gas that has similar molar weight and diffusion coefficient. The initial concentration of helium and oxygen in steam was 100 and 1000 times higher than in the real plant conditions in order to speed up the accumulation process. The non-condensables accumulation was detected with 143 thermo-couples along the pipeline inside. Results of the non-condensables accumulation and a possibility of the concentration front formation at several locations along the pipeline are presented in [2]. Pipeline's vertical segments and bends are indicated as possible locations of concentration fronts, and the non-condensables are accumulated in the volume of pipeline from the concentration front to the upper closed end. Required time periods for the concentration front propagation up to certain presented locations are not reported, neither are information about the dynamics of concentration front propagation along the pipeline. The non-condensables accumulation in the three-dimensional geometry of the RHRS pipeline was also numerically simulated with the one-phase computational fluid dynamic (CFD) model of the commercial code STAR-CD. In this modelling approach the steam condensation in the presence of non-condensables is taken into account through the mass sink term in the mass and momentum conservation equations. The condensate presence, drainage and influence on the gas mixture flow due to the gas mixture–condensate liquid film interfacial drag were not taken into account. One conservation equation for the mole concentration of the mixture of hydrogen

and oxygen was solved. Hence, no information about separate hydrogen and oxygen spatial concentration fields within the analyzed volumes could be obtained.

The radiolytic gases accumulation in the pressure impulse line connected to the reactor pressure vessel was analyzed in [5] with the lumped parameter model based on the macroscopic balances of the steam condensation, steam–radiolytic gases mixture inflow and outflow for defined control volumes along the non-vented pipe and corresponding radiolytic gases accumulation. Such an engineering approach is applicable to the simple pipe geometry and presents an approximate solution. It is not able to take into account recirculation flows and formation of vortexes within steam–non-condensables mixture in non-vented volumes. It is even possible that these methods could give misleading results regarding the formation and existence of explosive mixture formations. For instance, in case of nearly horizontal pipes, the buoyancy forces could lead to adequate venting of the pipe, which prevents a substantial non-condensables concentration increase and an explosive hydrogen–oxygen mixture formation [6]. In this case, the macroscopic balance approach will indicate explosive mixture accumulation. The other example is related to a vertical pipe closed at the top and open at the bottom. Again, one-dimensional or lumped parameter models are not able to predict steam–non-condensable gas mixture convection induced by buoyancy forces and interfacial shear at the condensate surface. Hence, these models are not able to predict sharp concentration and temperature change at the location of the propagating concentration front [7]. The results in [5] show continuous increase of non-condensables towards the closed end—the result that significantly deviates from the real conditions [7].

In order to investigate and predict the thermal-hydraulic, physicochemical and geometry conditions that lead to radiolytic gases accumulation, the HELIO code has been developed [6–8]. The HELIO code is based on the CMFD (computational multi-fluid dynamic) approach and it overcomes the deficiencies of the standard one-phase CFD approaches [2] or the approximate lumped parameter engineering calculations [5]. In the HELIO code the flow of gas mixture consisting of steam and radiolytic gases hydrogen and oxygen, as well as the steam condensate drainage are described with the two-fluid model, where a set of mass, momentum and energy conservation equation is written for each phase flow field. The mass transport of hydrogen and oxygen is described with the mass conservation equations written for each gas mixture component. The liquid and gas phases at the condensate liquid film surface are thermal-hydraulically coupled by the mass transfer due to the steam condensation and by imposing the same fluid velocity and fluid temperatures equal to the saturation temperature (determined with the steam partial pressure). The physicochemical coupling is performed through non-condensables absorption and degassing on the condensate film surface. In the HELIO code, the heat flux from the gas mixture to the environment is calculated by solving the three-dimensional transient heat conduction in the pipe's wall and insulator, or with the steady-state heat conduction through the pipeline wall and insulator in radial direction and with neglecting of the axial heat conduction (it was found that this second approach gives satisfactory results for the long duration pipeline transients, while the computing time is reduced). The solving procedure of the HELIO code is based on the SIMPLE type numerical method [9] modified for the conditions of two-phase flow [10]. A stable numerical solution of the liquid film flow is achieved by replacing the wall shear stress in pipe axial direction by the body force calculated with the one-dimensional model of liquid film–wall shear stress, by the introduction of the surface tension force, and by the application of the donor–acceptor numerical approach to the calculation of the liquid film volume fraction. The HELIO code has been used for the prediction of non-condensables accumulation in the vertical pipe under different boundary conditions [7,8,11] and for slightly inclined, nearly horizontal pipes [6]. Until now the HELIO code has been verified with available experimental data for the steam condensation in the presence of air in a flow over a vertical plate, and for the accumulation of radiolytic gases in a vertical non-vented pipe [8]. The comparison between HELIO code three-dimensional results and one-dimensional calculation for case of the radiolytic gases accumulation in vertical non-vented pipe closed at the top and open at the bottom is presented in [11]. For this simple geometry, both approaches give nearly the same amount of accumulated radiolytic gases, until the maximum non-condensables mass fraction of approximately 0.9 is reached. These results also contribute to the verification of the complex three-dimensional models applied in the HELIO code. But, as already stated in this Introduction, a substantial differences can be encountered between one and three-dimensional models for complex geometries.

The main goals of this paper are following: (a) to present developed thermal-hydraulic and physicochemical models and the corresponding numerical approach for the numerical simulation and analyses of complex three-dimensional processes of condensation induced radiolytic gases accumulation in non-vented pipelines; and (b) to verify the model against the available experimental data from the real geometry and conditions of the complex nuclear power plant pipeline. The presented model is unique since it comprises all important phenomena that affect the non-condensable gases accumulation in the mixture with condensing steam, and the model is verified against the real conditions of engineering importance. The presented three-dimensional numerical approach and results are the continuation of the HELIO code's development and testing presented in the previous paper [8] for two-dimensional axisymmetric pipe conditions. The geometry and operating parameters of the complex RHRS pipeline are outlined in Section 2. Section 3 presents the modelling approach. Sec-

tion 4 outlines a numerical solution procedure. Section 5 presents numerical results of the hydrogen and oxygen accumulation in a complex geometry of the RHRS pipeline of the Hamaoka NPP. The obtained three-dimensional transient results show the gas mixture temperature fields, the hydrogen and oxygen mass fraction fields, the propagation of the accumulated non-condensables front from the closed top towards the open bottom of the pipeline, the time rate of radiolytic gases accumulation, the condensate drainage, as well as the gas mixture convection induced by the steam condensation, by the buoyancy forces due to the non-uniform concentration and temperature fields and by the interfacial shear at the liquid film surface.

2. Problem statement

An example of the complex non-vented pipeline is shown in Fig. 1. Depicted configuration and dimensions correspond to the pipeline of the RHRS in the Hamaoka NPP. There is no forced flow through the pipeline, since the top of the pipeline is closed. The bottom is open. Initially, the pipeline is filled with the gas mixture of predominant steam and a small amount of radiolytic gases—hydrogen and oxygen. Although the pipeline is insulated, the heat loss to the surrounding cannot be eliminated, and steam condenses on the wall. The condensate is drained due to gravity in a form of the liquid film. Some amount of non-condensables is absorbed at the liquid film surface and removed with the drained condensate, but, regardless of this effect, the non-condensables concentration is increased due to the constant steam removal caused by the condensation. The condensed steam is replaced by the inflow of the mixture of steam and small amount of radiolytic gases at the junction of the pipeline bottom with the surrounding system. In this process, even an explosive hydrogen–oxygen concentration could be reached.

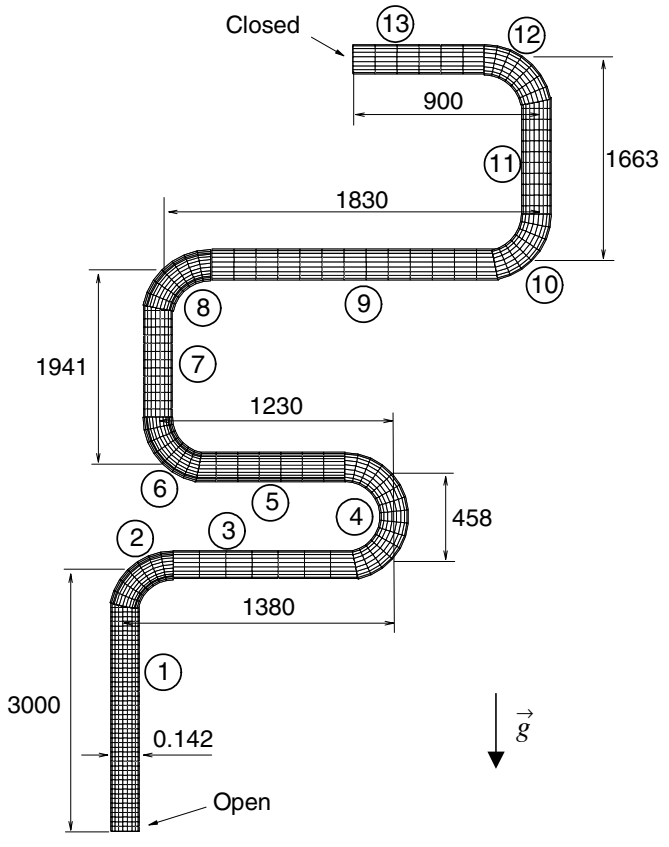

Fig. 1. Geometry of the pipeline of the Residual Heat Removal System in the Hamaoka Nuclear Power Plant and applied 3D numerical mesh (the segment numbers are circled; the numerical mesh consists of 10 control volumes in radial direction, 10 control volumes in circumferential direction, and the numbers of control volumes in longitudinal direction per segment are presented in Table 1).

A modelling of steam–non-condensables thermal-hydraulic and physicochemical conditions in non-vented pipelines has to take into account the following main phenomena: (a) mixture convection and circulation due to buoyancy forces induced by non-uniform concentration field of non-condensables, replenishment of the condensed steam by the mixture inflow at the open bottom, and interfacial drag between the gas mixture and the surface of the drained liquid film; (b) diffusion within the steam–hydrogen–oxygen mixture; (c) thin liquid film flow at the wall; (d) condensation in the presence of non-condensables; (e) absorption or degassing of non-condensables at the liquid film (it should be noted that besides the non-condensables absorption, it is also possible to have removal of non-condensable gases from the liquid film to the steam–non-condensables mixture if the non-condensables concentration in the liquid film is higher than the saturated concentration on the liquid film surface). These considerations have led to the formation of the thermal-hydraulic and physicochemical model, as described in the next section.

3. Modelling approach

Governing equations are written for two-phase flow, where the gas phase is a mixture of steam, hydrogen and oxygen, while the liquid phase is a condensate with dissolved non-condensable gases. Since the radiolytic gases accumulation is simulated for pipelines geometries, the mass, momentum and energy conservation equations are written in cylindrical coordinates for the general case of three-dimensional flow in a curved pipe, as shown in Fig. 2. The variable dynamic viscosity of the liquid and gas phase is considered. The conservation equations are written in the following form:

Mass conservation

$$\frac{\partial(\alpha_k\rho_k)}{\partial t}+\frac{1}{r}\frac{\partial(\alpha_k\rho_k r v_k)}{\partial r}+\frac{\partial(\alpha_k\rho_k u_k)}{\partial x}+\frac{1}{r}\frac{\partial(\alpha_k\rho_k w_k)}{\partial\theta}=(-1)^{k-1}\sum_{m=1}^{M}\Gamma_m \quad (1)$$

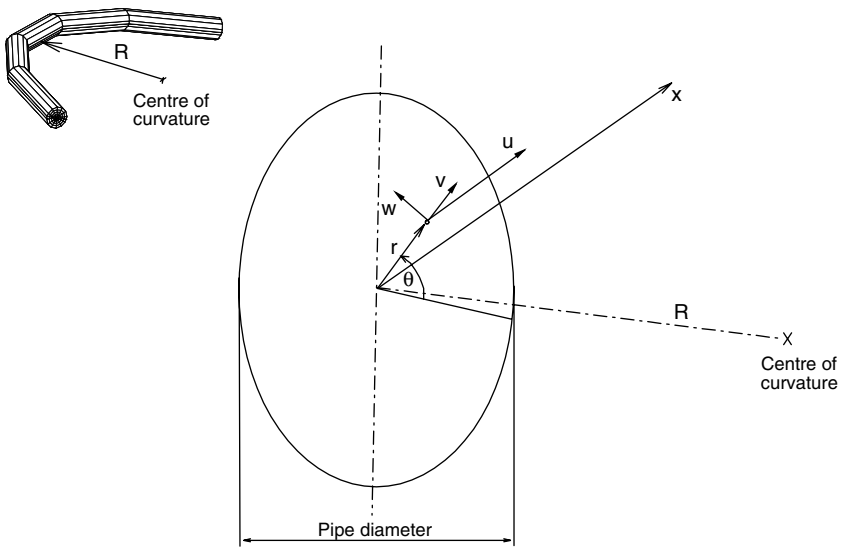

Fig. 2. Cylindrical coordinates and velocity components for the flow in a pipe elbow.

Momentum conservation

r-direction

$$\begin{aligned}
&\frac{\partial(\alpha_k\rho_k v_k)}{\partial t}+\frac{1}{r}\frac{\partial(\alpha_k\rho_k r v_k^2)}{\partial r}+\frac{\partial(\alpha_k\rho_k u_k v_k)}{\partial x}+\frac{1}{r}\frac{\partial(\alpha_k\rho_k v_k w_k)}{\partial\theta}\\
&\quad=-\alpha_k\frac{\partial p}{\partial r}+\frac{2}{r}\frac{\partial}{\partial r}\left(\alpha_k\mu_k r\frac{\partial v_k}{\partial r}\right)+\frac{\partial}{\partial x}\left(\alpha_k\mu_k\frac{\partial v_k}{\partial x}\right)\\
&\qquad+\frac{\partial}{\partial x}\left(\alpha_k\mu_k\frac{\partial u_k}{\partial r}\right)+\frac{1}{r}\frac{\partial}{\partial\theta}\left(\alpha_k\mu_k\frac{1}{r}\frac{\partial v_k}{\partial\theta}\right)\\
&\qquad+\frac{1}{r}\frac{\partial}{\partial\theta}\left(\alpha_k\mu_k r\frac{\partial}{\partial r}\left(\frac{w_k}{r}\right)\right)-2\alpha_k\mu_k\frac{1}{r^2}\frac{\partial w_k}{\partial\theta}\\
&\qquad-\frac{2\alpha_k\mu_k v_k}{r^2}+\frac{\alpha_k\rho_k w_k^2}{r}+(-1)^{k-1}\sum_{m=1}^{M}\Gamma_m v_i-\alpha_k\rho_k g_r\\
&\qquad-(k-2)F_\sigma-n\frac{\alpha_k\rho_k u_k^2}{R}\cos\theta
\end{aligned}\tag{2}$$

x-direction

$$\begin{aligned}
&\frac{\partial(\alpha_k\rho_k u_k)}{\partial t}+\frac{1}{r}\frac{\partial(\alpha_k\rho_k r u_k v_k)}{\partial r}+\frac{\partial(\alpha_k\rho_k u_k^2)}{\partial x}+\frac{1}{r}\frac{\partial(\alpha_k\rho_k u_k w_k)}{\partial\theta}\\
&\quad=-\alpha_k\frac{\partial p}{\partial x}+(k-1)\frac{1}{r}\frac{\partial}{\partial r}\left(\alpha_k\mu_k r\frac{\partial u_k}{\partial r}\right)\\
&\qquad+\frac{1}{r}\frac{\partial}{\partial r}\left(\alpha_k\mu_k r\frac{\partial v_k}{\partial x}\right)+2\frac{\partial}{\partial x}\left(\alpha_k\mu_k\frac{\partial u_k}{\partial x}\right)\\
&\qquad+\frac{1}{r}\frac{\partial}{\partial\theta}\left(\alpha_k\mu_k\frac{1}{r}\frac{\partial u_k}{\partial\theta}\right)+\frac{1}{r}\frac{\partial}{\partial\theta}\left(\alpha_k\mu_k\frac{\partial w_k}{\partial x}\right)\\
&\qquad+(-1)^{k-1}\sum_{m=1}^{M}\Gamma_m u_i-\alpha_k\rho_k g_x+(k-2)(a\tau)_{w,x}
\end{aligned}\tag{3}$$

θ-direction

$$\begin{aligned}
&\frac{\partial(\alpha_k\rho_k w_k)}{\partial t}+\frac{1}{r}\frac{\partial(\alpha_k\rho_k w_k^2)}{\partial\theta}+\frac{1}{r}\frac{\partial(\alpha_k\rho_k r v_k w_k)}{\partial r}+\frac{\partial(\alpha_k\rho_k u_k^2)}{\partial x}\\
&\quad=-\frac{\alpha_k}{r}\frac{\partial p}{\partial\theta}+\frac{2}{r^2}\frac{\partial(\alpha_k\mu_k v_k)}{\partial\theta}+\frac{2}{r}\frac{\partial}{\partial\theta}\left(\alpha_k\mu_k\frac{1}{r}\frac{\partial w_k}{\partial\theta}\right)\\
&\qquad+\frac{1}{r}\frac{\partial}{\partial r}\left(\alpha_k\mu_k r\frac{\partial w_k}{\partial r}\right)+\frac{1}{r^2}\frac{\partial}{\partial r}\left(\alpha_k\mu_k r\frac{\partial v_k}{\partial\theta}\right)\\
&\qquad+\frac{\partial}{\partial x}\left(\alpha_k\mu_k\frac{\partial w_k}{\partial x}\right)+\frac{\partial}{\partial x}\left(\alpha_k\mu_k\frac{1}{r}\frac{\partial u_k}{\partial\theta}\right)\\
&\qquad-\frac{\alpha_k\rho_k v_k w_k}{r}-\frac{\alpha_k\mu_k w_k}{r^2}+(-1)^{k-1}\sum_{m=1}^{M}\Gamma_m w_i\\
&\qquad-\alpha_k\rho_k g_\theta+n\frac{\alpha_k\rho_k u_k^2}{R}\sin\theta
\end{aligned}\tag{4}$$

Energy conservation

$$\begin{aligned}
&\frac{\partial(\alpha_k\rho_k c_{p,k}T_k)}{\partial t}+\frac{1}{r}\frac{\partial(\alpha_k\rho_k c_{p,k}r v_k T_k)}{\partial r}+\frac{\partial(\alpha_k\rho_k c_{p,k}u_k T_k)}{\partial x}\\
&\qquad+\frac{1}{r}\frac{\partial(\alpha_k\rho_k c_{p,k}w_k T_k)}{\partial\theta}\\
&\quad=\frac{1}{r}\frac{\partial}{\partial r}\left(\alpha_k k_k r\frac{\partial T_k}{\partial r}\right)+\frac{\partial}{\partial x}\left(\alpha_k k_k\frac{\partial T_k}{\partial x}\right)\\
&\qquad+\frac{1}{r}\frac{\partial}{\partial\theta}\left(\alpha_k k_k\frac{1}{r}\frac{\partial T_k}{\partial\theta}\right)+(-1)^{k-1}\sum_{m=1}^{M}\Gamma_m h_m
\end{aligned}\tag{5}$$

The parameters used in the above equations are the phase volume fraction α, phase density ρ, velocity components u, v and w, gas phase temperature T, pressure p (being the same in both phases), interfacial mass transfer rate due to phase transition or absorption/degassing Γ_m, dynamic viscosity μ, specific heat at constant pressure c_p, thermal diffusivity k. The index k denotes liquid film ($k=1$) or gas

mixture ($k = 2$). The parameter n in Eqs. (2) and (4) distinguishes between a straight pipe ($n = 0$) and a pipe elbow ($n = 1$). The radius of the pipe curvature is denoted with R. The last terms on the r.h.s. of Eqs. (2) and (4) represent the centrifugal force caused by the pipe curvature (these terms are zero in case of straight pipes).

Due to low heat losses from the gas mixture in insulated pipes to the surrounding atmosphere, the steam condensation rate is low, and consequently, the liquid film is thin (of the order of 1 mm or less). A calculation of the velocity or temperature distribution across the film thickness (i.e. in a direction perpendicular to the liquid film surface) is not practically achievable; such an approach would require a several control volumes within the film thickness (which means that the total number of numerical control volumes must be increased within the pipe), and that would prolong the computational time substantially without the engineering rationale for that. Therefore, the whole thickness of the condensate film is usually comprised within one control volume. For such an approach, it has been shown that a stable calculation of the condensate film flow on the wall is achieved by replacing the viscosity diffusion term in the axial direction (the second term on the r.h.s. of Eq. (3)), with a body force (the last term in Eq. (3)) determined with one-dimensional model, as it is described below.

In Eq. (3) the product $(a\tau)_{w,x}$ represents the liquid film–wall shear force per unit volume, where a represents the interfacial area concentration in (m^{-1}) and τ is the shear stress in ($N\,m^{-2}$). By assuming that the liquid film surface is parallel to the wall, the specific interfacial area is calculated as

$$a = \frac{\Delta x\,\Delta\theta(r_w - \delta_1)}{\Delta x\pi\left[r_w^2 - (r_w - \Delta r)^2\right]\Delta\theta/(2\pi)} = \frac{(r_w - \delta_1)}{r_w\Delta r - 0.5(\Delta r)^2} \approx \frac{1}{\Delta r} \tag{6}$$

where in Eq. (6) it is taken into account that the pipe inner radius is much greater that the liquid film thickness $r_w \gg \delta_1$, and $(\Delta r)^2 \to 0$. The corresponding expression for the wall shear stress in x-direction is

$$\tau_{w,x} = f_{w,x}\frac{\rho_1 u_1^2}{2} \tag{7}$$

where the friction coefficient for the assumed laminar flow of the thin liquid film is calculated as

$$f_{w,x} = \frac{16}{Re_{1,x}} \tag{8}$$

the liquid film Reynolds number is

$$Re_{1,x} = \frac{\rho_1 u_1 D_{h1}}{\mu_1} \tag{9}$$

and the hydraulic diameter for the liquid film is

$$D_{h1} = \frac{4A_1}{S_{1w}} \approx \frac{4\pi D\delta_1}{\pi D} = 4\delta_1 \tag{10}$$

Due to the low liquid film thickness and velocity, the laminar film flow is assumed.

In the momentum conservation Eqs. (2)–(4) for the thin liquid film, the interfacial shear stress between the liquid film and the gas mixture is neglected, since in [8] it was shown that the interfacial shear stress that acts on the liquid film is significantly lower than the wall shear stress, namely

$$\frac{\tau_w}{\tau_i} = \frac{\rho_1 g\delta_1 D}{8\mu_2(u_2 - u_1)} \tag{11}$$

which for the conditions of pure steam at the pressure level of 7 MPa in the pipe with a large diameter of $D = 0.1$ m gives

$$\frac{\tau_w}{\tau_i} = \frac{740\cdot 9.81\cdot 50\cdot 10^{-6}\cdot 0.1}{8\cdot 20\cdot 10^{-6}|u_2 - u_1|} \approx \frac{230}{|u_2 - u_1|} \tag{12}$$

In non-vented and insulated pipes the gas mixture and liquid film velocities are lower than 1 m s^{-1} (usually much lower), which means that the interfacial shear stress is negligible compared to the wall shear stress.

The liquid film velocity boundary conditions imply no-slip conditions on the wall, while the gas mixture–liquid film interfacial velocity is equal to the liquid film surface velocity.

In order to preserve the liquid film surface in the vicinity of the wall, the surface tension force is introduced in Eq. (2) as a body force acting in the direction of the pipe radius

$$\vec{F}_\sigma = a_{12}\frac{2\sigma}{D}\vec{r} \tag{13}$$

where a_{12} is calculated with Eq. (6). A presentation of the surface tension with the volume body force is the common numerical technique in methods for the interface tracking in multi-phase flows [12].

Application of the mass, momentum and energy conservation Eqs. (1)–(5) for the thin film flow of condensate on the wall, with the numerical grid that is not refined across the film thickness, means that the calculation of the averaged liquid film parameters across the film thickness is of interest (such as mean liquid film thickness, mean film temperature and mean velocity). Local changes, such as a wavy liquid film behaviour or a temperature change across the water film of the order lower than 1 mm may be neglected in regard to the bulk phenomena of interest (for instance the liquid film thermal resistance is negligible compared to the thermal resistance of the pipe insulator or non-condensables layer adjacent to the pipe wall, or the liquid film wavy behaviour is not essential for the integral rate of liquid film drainage on the wall, as long as the wall friction factor is correctly predicted).

The volume fraction balance of the gas and liquid phase is

$$\alpha_1 + \alpha_2 = 1 \tag{14}$$

The sum of interfacial mass transfer rates in Eqs. (1)–(5) is written as

$$\sum_{m=1}^{M} \Gamma_m = \Gamma_{\mathrm{con}} + \Gamma_{\mathrm{a,H_2}} + \Gamma_{\mathrm{a,O_2}} \tag{15}$$

The steam condensation rate is denoted as Γ_{con}, while terms $\Gamma_{\mathrm{a,H_2}}$ and $\Gamma_{\mathrm{a,O_2}}$ represent absorption ($\Gamma_{\mathrm{a,c}} > 0$, $\mathrm{c} = \mathrm{H_2}$, $\mathrm{O_2}$) or degassing ($\Gamma_{\mathrm{a,c}} < 0$) rates of hydrogen and oxygen per unit volume respectively. Components of the gas mixture and liquid phase interfacial velocity, where condensation, absorption or degassing take place, are denoted with u_i, v_i and w_i, and they are equal to the corresponding liquid film velocity components.

Hydrogen and oxygen convection and diffusion in the mixture with steam are treated for each component separately; therefore, the mass fraction conservation equation is written and solved for each non-condensable component. In three-dimensional cylindrical coordinates mass fraction conservation equation has the following form:

$$\begin{aligned}
&\frac{\partial(\alpha_2\rho_2 g_{\mathrm{c},2})}{\partial t} + \frac{1}{r}\frac{\partial(\alpha_2\rho_2 r v_2 g_{\mathrm{c},2})}{\partial r} + \frac{\partial(\alpha_2\rho_2 u_2 g_{\mathrm{c},2})}{\partial x} \\
&\quad + \frac{1}{r}\frac{\partial(\alpha_2\rho_2 w_2 g_{\mathrm{c},2})}{\partial \theta} \\
&\quad = \frac{1}{r}\frac{\partial}{\partial r}\left[\alpha_2\rho_2 r D_{\mathrm{c}}\frac{\partial g_{\mathrm{c},2}}{\partial r}\right] + \frac{\partial}{\partial x}\left[\alpha_2\rho_2 D_{\mathrm{c}}\frac{\partial g_{\mathrm{c},2}}{\partial x}\right] \\
&\qquad + \frac{1}{r}\frac{\partial}{\partial \theta}\left[\alpha_2\rho_2\frac{1}{r}D_{\mathrm{c}}\frac{\partial g_{\mathrm{c},2}}{\partial \theta}\right] - \Gamma_{\mathrm{a,c}}
\end{aligned} \tag{16}$$

The index c in Eq. (16) denotes the non-condensable component (hydrogen or oxygen). The non-condensable mass fraction is denoted as g, while the diffusion coefficient of non-condensable component c in the gas mixture is denoted with D_{c}. At the liquid film surface the non-condensable sink due to the absorption is taken into account through the $\Gamma_{\mathrm{a,c}}$ term, while no change of non-condensable mass fraction in radial direction is assumed in control volume that comprise liquid film surface. The hydrogen diffusion through the pipe's metal wall and its removal by this mechanism from the pipeline inner volume to the surrounding atmosphere is neglected since the gas transport by diffusion through solids is negligible compared to diffusion in liquids, for instance the diffusion coefficient of hydrogen in iron is $2.6\times10^{-13}\ \mathrm{m^2\ s^{-1}}$, while for a diffusion in water it is $4.5\times10^{-9}\ \mathrm{m^2\ s^{-1}}$ at 20 °C [14].

According to the analyses presented in [8] it is assumed that the thin condensate liquid film is saturated with non-condensables. It is shown that due to the small film thickness, the value of the mass transfer coefficient and mass transfer rates of non-condensables from the gas mixture to the liquid film are high enough to provide saturated non-condensables concentration in the condensate film. Hence, the non-condensables absorption from the gas mixture to the condensate film, or the non-condensables degassing from the film to the gas mixture is calculated from Eq. (16) by assuming that (a) the non-condensables mass fraction equals the saturated value determined with the Henry's law [14], (b) the non-condensables transport by diffusion in the liquid is much lower than its transport by convection [13], and (c) the mass fraction change across the thin liquid film is neglected. Under these assumptions the following equation is derived from Eq. (16)

$$\Gamma_{\mathrm{a,c}} = \frac{\partial(\alpha_1\rho_1 g_{\mathrm{c},1})}{\partial t} + \frac{\partial(\alpha_1\rho_1 u_1 g_{\mathrm{c},1})}{\partial x} + \frac{1}{r}\frac{\partial(\alpha_1\rho_1 w_1 g_{\mathrm{c},1})}{\partial \theta} \tag{17}$$

According to the procedure described in [8] the mean non-condensables mass fraction in the liquid film is calculated with

$$g_{\mathrm{c},1} = g_{\mathrm{c},2,i}\frac{p}{H_{\mathrm{c}}}\frac{M_{2,i}}{M_{1,i}} \tag{18}$$

Eq. (18) is derived in [8] from the Henry's law,

$$x_{\mathrm{c},1,i} = \frac{p_{\mathrm{c},i}}{H_{\mathrm{c}}} \tag{19}$$

by introducing the simple relation between the non-condensable molar and mass fractions

$$x_{\mathrm{c},1,i} = g_{\mathrm{c},1}\frac{M_{1,i}}{M_{\mathrm{c}}} \tag{20}$$

and the relation between the non-condensable partial pressure in the gas mixture and the mass fraction on the gas side of the gas–liquid film interface

$$p_{\mathrm{c},i} = g_{\mathrm{c},2,i}p\frac{M_{2,i}}{M_{\mathrm{c}}} \tag{21}$$

The Henry's law (Eq. (19)) states that the molar fraction of absorbed non-condensable gas at the liquid surface $x_{\mathrm{c},1,i}$ is related to the non-condensable partial pressure in the gas mixture $p_{\mathrm{c},i}$. The Henry's law is applicable when the concentration of non-condensable on the liquid surface reaches equilibrium and for a small concentration of non-condensable in the liquid (it should be noted that both these conditions are approximately satisfied in the transient non-condensables accumulation process treated in this paper, the time periods of the accumulation process is very long, so it is assumed that the equilibrium of non-condensables concentration exists between the gas and liquid phase, and the solution of hydrogen and oxygen in water is dilute). The Henry's constant H_{c} for the non-condensable c in Eq. (19) in fact depends on the pair of dissolved non-condensable gas and liquid, on the equilibrium gas–liquid temperature and on the non-condensable partial pressure. In this paper the Henry's constant $H_{\mathrm{O_2}}$ of oxygen in water is calculated with the empirical correlation proposed in [15] and already applied in [8], as a function of the partial pressure of oxygen in the gas mixture and liquid film temperature. The Henry's constant strongly depends on temperature and weakly on pressure, as it is depicted in Fig. 3. Data on the Henry's constant of hydrogen in water at elevated pressures and temperatures are not available in the open literature, while the relative difference of hydrogen to oxygen Henry's constant for water is approximately 10% at moderate pressures and temperatures [14]. Thus, the Henry's constant of hydrogen in water is assumed to be equal to that of oxygen.

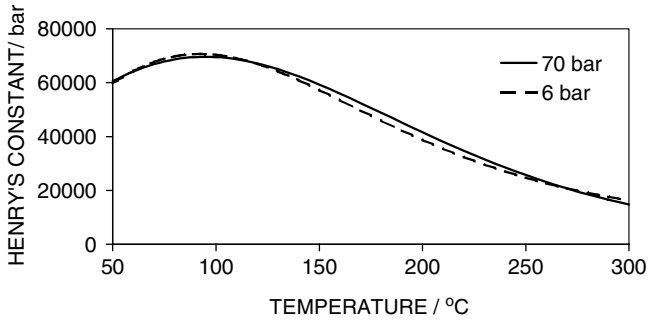

Fig. 3. Dependence of Henry's constant on pressure and temperature calculated according to [15].

The thermal-hydraulic processes in the gas mixture of steam and non-condensables in the non-vented pipe interact with the transient heat conduction in the pipe's wall and insulator (as explained the resistance to the heat transfer across the thin liquid film is neglected). The existence of the condensation or heat convection mechanisms and corresponding intensity of the heat transfer on the inside pipe's wall surface is determined by the relation of the saturation temperature (determined with the steam partial pressure in the gas mixture) and the inside wall surface temperature, which is the result of coupled flow, mass and thermal transport processes on the gas mixture side and the transient axial, radial and circumferential heat conduction in the pipe's wall and insulator. The general approach applied to the calculation of the heat losses from the gas mixture inside the pipeline to the ambient atmosphere in the HELIO code implies the numerical solving of the transient three-dimensional Fourier heat conduction equation in cylindrical coordinates. But, since the non-condensables accumulation processes are very slow (last for days, weeks or even months), the influence of the transient character of the heat conduction in the pipe's wall and insulator on the non-condensables accumulation is usually negligible. Also, the heat conduction in the radial direction is dominant, except at the location of the concentration front, where a temperature difference of tens or even a hundred degrees Celsius can be reached in the gas mixture, and the axial heat conduction in the pipe wall takes place in the vicinity of the front. But, in cases of long pipelines (several meters or more), the wall axial heat conduction at the location of the concentration front and its influence on the front location can be neglected in regard to the whole pipe length. The axial heat conduction in the pipe wall can be important also at the pipe ends if adiabatic boundary conditions are not valid, but these kinds of boundary conditions (such as prescribed temperature at the pipe end or prescribed heat flux) are not applied to the conditions simulated in this paper. These assumptions led to the application of the simple prediction of only radial steady-state heat conduction in case of the long pipeline. In this way, the replacing of the solving of the transient Fourier three-dimensional equation with the simple algebraic relations reduces the already long computational time without the violation of the reliability of obtained results.

Heat can be transferred from the mixture of non-condensables and steam to the pipe's wall by the mechanisms of steam condensation and convection or only by convection. Condensation exists if the local steam saturation temperature at the pipe wall (determined with the local steam partial pressure in the gas mixture) is higher than the inner pipe wall surface temperature. The thermal boundary condition at the pipe inner wall, in case without the steam condensation, is determined with the equality of the heat fluxes on the gas mixture and wall side

$$-k_2 \frac{\partial T_2}{\partial y} = q_A \quad \text{at } r = r_{w1} \tag{22}$$

where k_2 is the thermal conductivity of the gas mixture at the wall surface, T_2 is the gas mixture temperature, and q_A is the radial heat flux through the wall and insulator. The radii of the pipe wall and insulator inner and outer surfaces are depicted in Fig. 4. In case with the condensation on the wall inner surface, the wall inner surface temperature is equalised to the liquid film temperature in the control volume on the wall

$$T_w = T_1 \quad \text{at } r = r_{w1} \tag{23}$$

The temperature at the liquid film surface is equal to the steam saturation temperature determined with the steam partial pressure

$$T_1 = T_{sat.}(p_{steam}) \quad \text{at } r = r_{w1} - \delta_1 \tag{24}$$

If the whole liquid film is comprised within one control volume adjacent to the pipe wall, then the heat transfer across the liquid film thickness is not considered and it equals the steam saturation temperature.

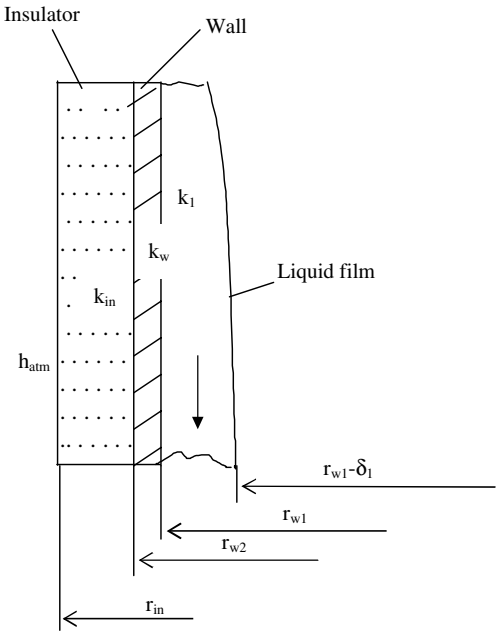

Fig. 4. Characteristic dimensions of the pipe wall and insulator.

The boundary condition stated with Eq. (24) neglects the temperature jump on the gas mixture–liquid film interface. This assumption is justified for atmospheric or higher pressures [16]. The steam partial pressure p_{steam} in Eq. (24) is determined with the Dalton's law

$$p_{steam} = p - p_{H_2} - p_{O_2} \tag{25}$$

and the partial pressures of hydrogen and oxygen are determined with Eq. (21)

Radial steady-state heat conduction is calculated as

$$q_A = k_{overall}(T_{w,r=r_{w1}} - T_{atm}) \tag{26}$$

where the overall heat transfer coefficient calculated at r_{w1} is equal to

$$k_{overall} = \frac{1}{\frac{r_{w1}}{k_w}\ln\frac{r_{w2}}{r_{w1}} + \frac{r_{w1}}{k_{in}}\ln\frac{r_{in}}{r_{w2}} + \frac{r_{w1}}{r_{in}h_{atm}}} \tag{27}$$

The condensation rate is determined as

$$\Gamma_{con} = q_A A_i/(\lambda V_{CV}) \tag{28}$$

The possibility that a part of the pipe length is not covered with the insulator or that there is no insulator at all around the pipe wall is included in the model.

The gas mixture density is calculated as the sum of the component densities. The steam density is calculated as a function of temperature and pressure with appropriate polynomials developed on the basis of steam tables [17]. The oxygen and hydrogen densities are calculated from the ideal gas law. Gas mixture and component densities are depicted for the pressure of 7 MPa in Fig. 5, assuming that the steam is saturated, that the mixture components are in the thermal equilibrium, and that the mole ratio of hydrogen to oxygen is 2:1. The right end of the curve corresponds to the negligible amount of radiolytic gases (the steam saturation temperature at 7 MPa is 285.8 °C), while the left end corresponds to the negligible amount of steam in the mixture (the steam saturation temperature at pressure of approximately 0.03 bar is 25 °C). The mixture density curve has a minimum at approximately 185 °C. This characteristic dependence has the influence on the induction of buoyancy forces in the gas mixture. For temperatures higher than 185 °C the gas mixture flow is self-organized from the areas of higher temperature to the areas of lower temperatures due to the induced buoyancy forces; the opposite holds for the temperatures lower than 185 °C.

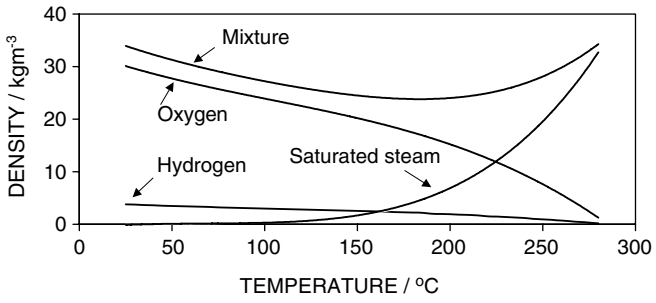

Fig. 5. Gas mixture and components densities at 7 MPa.

In the calculation of diffusion coefficients in the ternary steam–oxygen–hydrogen gas mixture, the appropriate coefficients of diffusion in binary mixtures are calculated with the Gilliland relation, while the diffusion coefficient of component c in a multi-component gas mixture (three or more components in the mixture), D_c, is calculated with the Wilky's formula [14,18,19]. The gas mixture dynamic viscosity, specific heat and thermal conductivity are calculated according to [19]. These procedures for the calculation of thermo-physical and diffusion parameters were already described and applied in [8]. The semi-empirical correlations applied for the prediction of transport properties of steam–hydrogen–oxygen ternary mixture provide acceptable accuracy for low and moderate pressures, while at the high pressure their predictions could deviate from experimental data. Since here developed three-dimensional model is applied to very slow transients, and the main purpose of the modelling is the temporal and spatial prediction of the radiolytic gases accumulation, it can be argued that these uncertainties of the transport properties have influence only on the accumulation of non-condensables through the uncertainty of diffusion coefficient values, mainly near the concentration front, while other influences on velocity or temperature fields are smeared due to the very slow development of the transient. For instance, no substantial changes of temperature and radiolytic gases mass fraction within the non-vented pipes' cross sections are observed in simulated experiments. But, the comparison of the HELIO code results with the available experimental data and the achieved agreement justifies the applied modelling approach (as demonstrated in Section 5 of this paper).

4. Numerical method

The system of governing Eqs. (1)–(5), (16) is discretized for control volumes in cylindrical coordinates. The scalar parameters, such as pressure, temperature, and non-condensable mass fractions are calculated for the basic (scalar) control volumes, while the velocity components are calculated for staggered control volumes [9]. The convective and diffusive terms at the control volume boundaries are determined with the power low numerical scheme as presented in [9]. Fully implicit time integration is applied. The pressure field is calculated according to a modified SIMPLE numerical method that takes into account the presence of two phases—liquid and gas, as presented in [10]. The resulting set of discretized equations is solved iteratively by the alternating direction implicit (ADI) method.

The iterative calculation procedure is performed as follows:

1. Gas mixture and liquid film temperatures, non-condensables' mass fractions and liquid film volume fractions are calculated for scalar control volumes.

2. Gas mixture velocity components are calculated for staggered control volumes.
3. Liquid film velocity components are calculated for staggered control volumes.
4. Pressure correction equation is solved for scalar control volumes.
5. Gas mixture and liquid film velocities are corrected with the pressure correction values.
6. If the error of the mass balance in all scalar control volumes is lower than the prescribed value, the program execution continues with the next step, otherwise the time step is divided by two, the current values of dependent variables are equalled to the initial ones and the program execution is returned to step 1.
7. The time is increased, new values of dependent variables are assigned to initial ones for the new time step of integration and the physical properties are updated with the new values of the dependant variables.
8. If the end of the transient is reached the program execution is stopped, otherwise the program execution continues with step 1.

In order to diminish the condensate film smearing across the computational domain, the additional donor–acceptor restriction is introduced; if the volume fraction of the phase in the donor cell is lower than 10^{-6}, the phase velocity across the cell boundary is zero [20].

The convergence of the numerical procedure is achieved by performing the calculation within the prescribed errors for inner and outer iterations. The set of algebraic equations obtained by the discretization of one conservation equation is solved within the inner iterations. The inner iterations are performed until the maximal difference of calculated dependent variable in two consecutive iterations in all control volumes is less than prescribed error. This criterion is satisfied in the calculation of all variables. The outer iterations are applied to the solving of all sets of discretized governing equations. By the solving of pressure correction equation, the maximum error of mass balance for all scalar control volumes is determined. The outer iterations are performed until the maximum mass balance error is lower than the prescribed error. If this criterion cannot be satisfied for certain acceptable number of outer iterations, the time step of integration is reduced by two and the solution procedure is repeated.

In order to achieve a required accuracy of the calculation with smaller number of iterations, the correction of the inlet gas mixture velocity at the open pipeline end is introduced as follows:

$$u^{t+\Delta t}_{\mathrm{inlet},0} = u^{t}_{\mathrm{inlet}} \frac{\int_V \frac{\Gamma^t_{\mathrm{con}}}{\rho^t_2} \mathrm{d}V}{\int_A u^t_{\mathrm{inlet}} \mathrm{d}A} \tag{29}$$

where $u^{t+\Delta t}_{\mathrm{inlet},0}$ is the initial value of inlet gas velocity at the open end of the pipeline for the new time step of integration $t+\Delta t$, u^t_{inlet} is the calculated value of the inlet gas velocity for the previous time step of integration t, the volume integral represents the sink of gas volume due to steam condensation, while the surface integral calculates the volume of inlet gas mixture that replenishes the volume of condensed steam. The correction according to Eq. (29) reduces the error of mass balance calculation and thus increases the overall accuracy of the calculation.

The stability of the numerical procedure depends on the dynamics of thermal-hydraulic processes of gas mixture and condensate flow and on the transient heat conduction in the pipes' walls and insulators. The flow of gas and condensate impose the maximum allowed time step of integration during the transient according to the Courant criterion

$$\Delta t < \min \left(\frac{\Delta x}{u}, \frac{\Delta r}{v}, \frac{r\Delta\theta}{w} \right)_{i,j,k} \tag{30}$$

where this criterion is applied to the flow of both phases and for all nodes (i,j,k) and the lowest calculated value of Δt is adopted as the maximum allowed time step of integration. Although the implicit numerical solution procedure is applied, the smaller integration time step is provided by the Courant criterion in order to serve as the underrelaxation parameter, which provides stability of the numerical method for here simulated highly non-linear conditions [9].

5. Results and discussion

The developed approach to the modelling and simulation of the non-condensable radiolytic gases hydrogen and oxygen accumulation in pipelines is applied to the prediction of hydrogen transient that occurred in the pipeline of the Residual Heat Removal System in the Hamaoka Nuclear Power Plant. The pipeline geometry is shown in Fig. 1 and Table 1 together with the applied three-dimensional numerical mesh. The total number of applied pipeline segments that consist of straight pipes and pipe elbows is 13 and the total length of the simulated pipeline

Table 1
Numbers of control volumes in axial direction per each segment of the pipeline shown in Fig. 1 and the lengths from the closed end to the segments' inlets

Segment number (see Fig. 1)	Number of control volumes in axial direction	The length from the closed pipeline end to the segment inlet (m)
1	50	12.02
2	8	9.02
3	8	8.66
4	15	7.74
5	8	7.01
6	8	6.24
7	15	5.88
8	8	4.38
9	14	4.02
10	8	2.62
11	12	2.26
12	8	1.06
13	7	0.70

is 12 m. The pipeline top end is closed, while the bottom end is open. The gas mixture pressure at the open end is 7 MPa. The initial values of hydrogen and oxygen mass fractions in the mixture with steam and their inflow values at the open pipe boundary are respectively 2.0×10^{-3} and 16×10^{-3}. These values are the same as applied in the physical experiments described in [2]. These initial radiolytic gases concentrations are intentionally taken to be 1000 times higher than in the real situation at the plant, in order to speed up the experimental procedure. The heat losses from the pipeline to the surrounding atmosphere are not presented in [2]. Hence, the overall heat transfer coefficient from the pipeline inside to the surrounding atmosphere is estimated. The overall heat transfer coefficient is influenced by the thermal conductivity in the pipeline insulator and by the natural convection from the insulator outer surface to the surrounding atmosphere, while the heat conduction in the pipeline metal wall and the heat transfer across the thin condensate film impose negligible heat resistance compared with the insulator conduction and outer natural convection. The value of the thermal conductivity coefficient for the insulator is estimated in the range from 0.05 to 0.1 $W\,m^{-1}\,K^{-1}$, the insulator thickness is in the range of several centimeters, while the heat transfer coefficient at the insulator surface to the surrounding atmosphere is expected to be not higher than 5 $W\,m^{-2}\,K^{-1}$. According to Eq. (27) the overall heat transfer coefficient is estimated in the range from 1 to 4 $W\,m^{-2}\,K^{-1}$. A value of 4 $W\,m^{-2}\,K^{-1}$ is adopted in this paper for the referent calculation. A simulation is also performed with a value of 33 $W\,m^{-2}\,K^{-1}$ in order to test the influence of the intensity of heat losses on the non-condensables front formation and propagation along the pipeline, as well as on the code accuracy and robustness of the calculation. The surrounding atmosphere is assumed to be at 25 °C. The adiabatic heat conduction condition is prescribed for closed pipe end, while the inlet temperature of the steam–non-condensables gas mixture at the open end is equal to the steam saturation

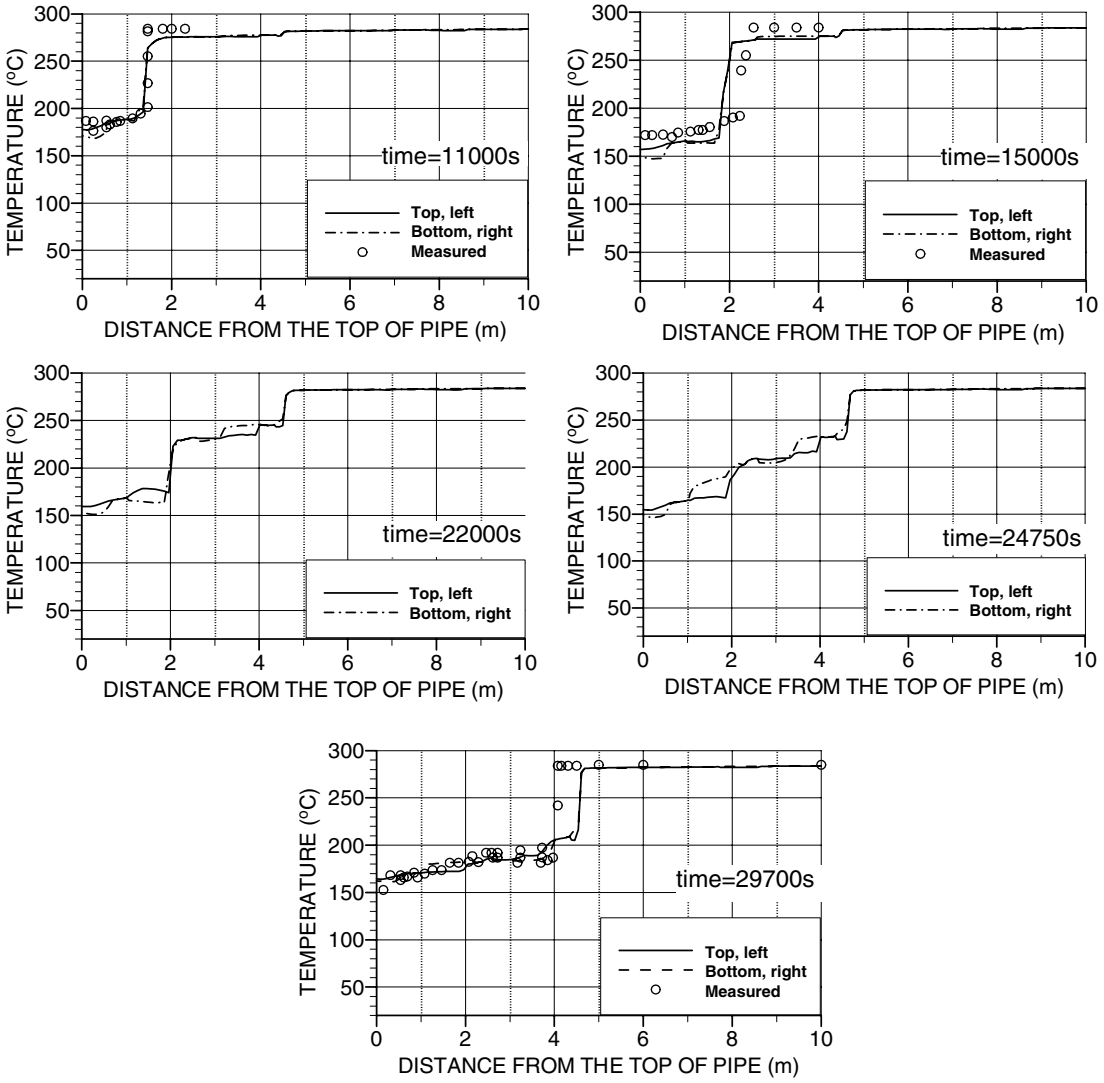

Fig. 6. Propagation of the radiolytic gases concentration front under the overall heat transfer coefficient of 4 $W\,m^{-2}\,K^{-1}$.

temperature according to the steam partial pressure. The velocity boundary conditions are specified through the no-slip conditions of the liquid film velocity on the wall. At the pipeline open end there is no change of the gas mixture axial velocity component, while the radial and circumferential velocity components are equal to zero. In order to avoid a counter-current gas mixture and liquid film flow at the pipeline open bottom end, which leads to a calculation instability and a substantial increase of the calculation errors of the velocity field, it is assumed that the pipe is adiabatically insulated 0.6 m from the bottom and the whole liquid film flow is removed in the control volumes at the location of 0.6 m from the pipe bottom.

The propagation of the radiolytic gases concentration front is shown in Fig. 6 with the temperature profile along the pipeline. The temperature change at the top of the horizontal pipe segments and the left sides of the vertical pipes is drawn with the full line. The dashed line presents temperature at the bottom of the horizontal segments and the right sides of the vertical pipes. Top, bottom, right and left positions are indicated in Fig. 7. For temperatures above 185 °C, a mixture with higher concentration of the accumulated radiolytical gases has a lower density (as presented in Fig. 5), which leads to lower top than bottom temperatures in the horizontal pipe segments. The reverse holds for temperatures lower than 185 °C. Results in Fig. 6 for 11,000 s and 15,000 s show that the concentration front is first formed in the vertical segment 11 (see Fig. 1), and then it is moved to the top part of the vertical segment 7 (Fig. 1) as presented for time instant 29,700 s. Since this calculation is performed with 1000 times higher values of the hydrogen and oxygen concentrations in the gas mixture inflowing into the pipeline and in the initial gas mixture in the pipeline, the calculated accumulation period is 1000 times shorter than the real process at the plant for the same amount of accumulated radiolytic gases. Hence, here presented and calculated time period of 8.25 h in the bottom picture of Fig. 6 corresponds to approximately 8250 h in real plant conditions. That means that in order to have the propagation of the concentration front approximately 4.5 m from the closed pipeline top end, the accumulation process should last about 340 days. Due to this long accumulation period it should be expected that the radiolytic gases concentration front did not propagate further from segment 7 (Fig. 1) during the Hamaoka NPP incident, and the hydrogen–oxygen explosion should be initiated somewhere within segments 8–13. As shown in Fig. 6 the calculated temperature profiles are compared with available measured data. The acceptable agreement is obtained. Both profiles have the same shape, while some discrepancy in the location of the concentration front, shown by the abrupt temperature change, for the latter periods of 15,000 s and 29,700 s could be attributed to differences in complex boundary conditions applied in the calculation scenario and during the course of the performed experiment at the test facility. Time periods of accumulation were not reported in [2]. The calculated temperature field after 29,700 s of the accumulation process is shown in Fig. 7 for the referent heat loss flux of 4 W m^{-2} K^{-1}. The accumulation of hydrogen and oxygen at the closed pipeline end leads to a temperature decrease to the value of approximately 150 °C in the horizontal segment 13 at the top. The stable concentration front is formed at the location of approximately 4.5 m from the closed pipeline top end (a location in the upper part of the vertical segment 7), which results in the sharp temperature change. The decrease of the gas mixture temperature due to the radiolytic gases accumulation also results in the decrease of the heat losses from the pipeline to the surrounding atmosphere (the gas mixture-outside temperature difference is lower), and, hence, the condensation rate within the pipe is decreasing during the transient accumulation.

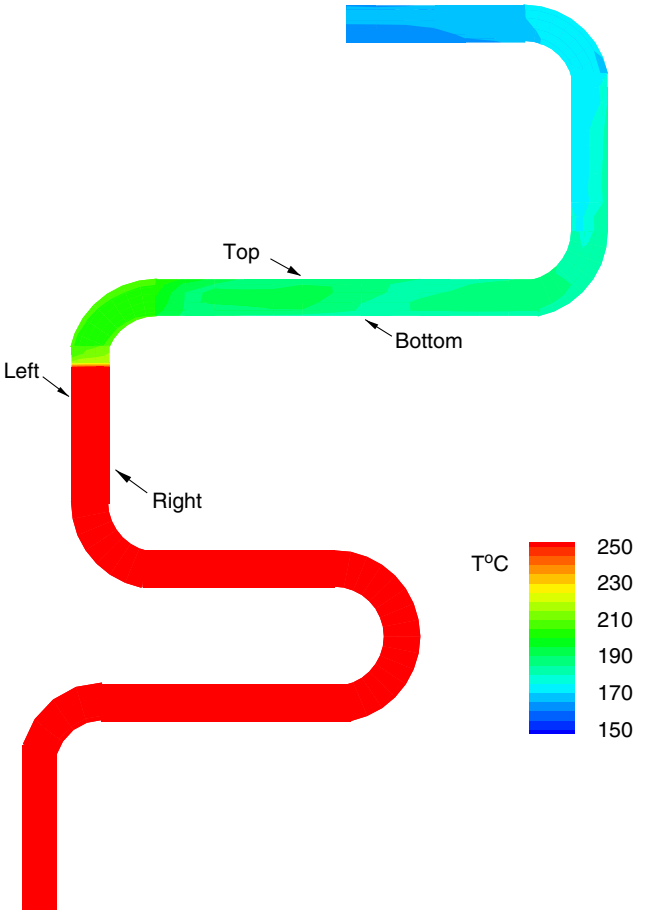

Fig. 7. Temperature change in the pipeline of the RHR system in Hamaoka NPP due to the radiolytic gases accumulation after 8 h (overall heat transfer coefficient is 4 W m^{-2} K^{-1}).

In order to investigate the influence of the heat loss intensity on the dynamics of the radiolytic gases accumulation, on the concentration front propagation and on the accuracy and robustness of the calculation procedure, the transient is also simulated with the higher value of the overall heat transfer coefficient of 33 W m^{-2} K^{-1}. Calculated temperature profiles along the pipeline are shown in Fig. 8. In this case of higher heat losses to the surrounding,

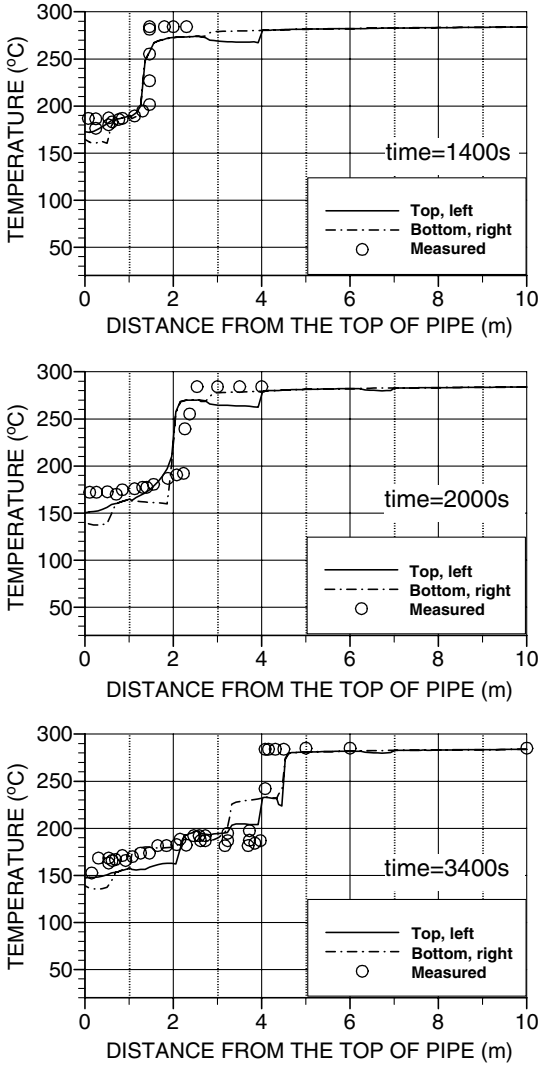

Fig. 8. Propagation of the radiolytic gases concentration front under the overall heat transfer coefficient of 33 W m^{-2} K^{-1}.

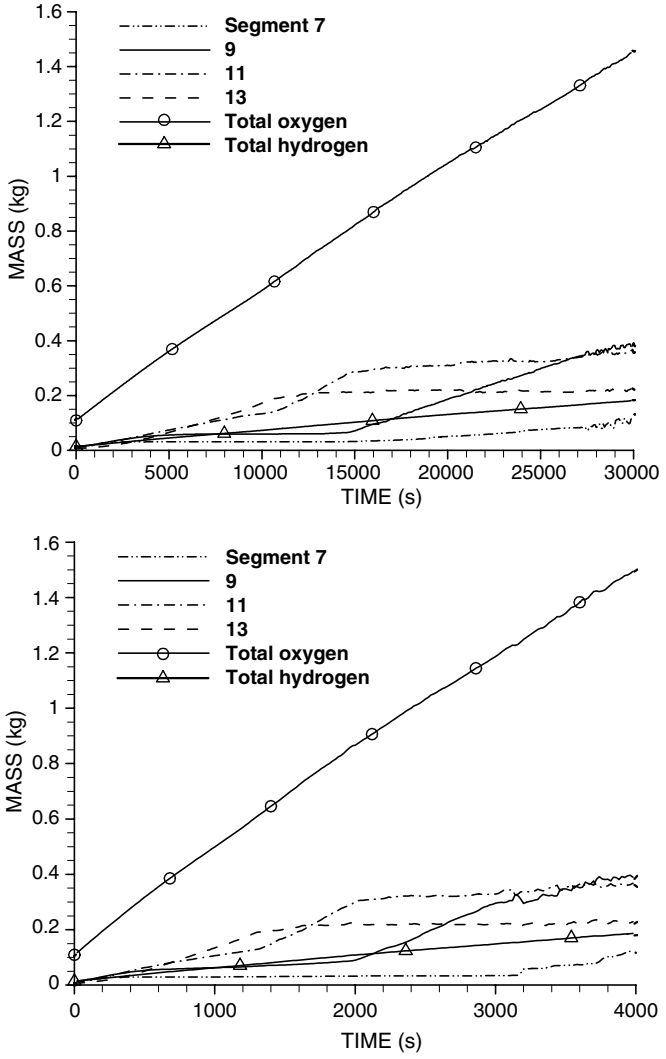

Fig. 9. Masses of accumulated hydrogen and oxygen in the whole pipeline and in some segments (overall heat transfer coefficient is 4 W m^{-2} K^{-1}—top, 33 W m^{-2} K^{-1}—bottom).

the concentration front propagates faster than in case with lower heat flux of 4 W m^{-2} K^{-1} presented in Fig. 6. Comparing the corresponding time periods of concentration front propagation to three measured locations in Figs. 6 and 8, the following ratios are read: 11,000 s:1400 s, 15,000 s:2000 s and 29,700 s:3400 s, and they are approximately the same as the ratio of the applied heat transfer coefficients 33 W m^{-2} K^{-1}:4 W m^{-2} K^{-1}. This implies that the accumulation time can be linearly correlated with the heat transfer coefficient. This is an important conclusion since a long calculation time can be substantially reduced by applying a higher value of the heat loss coefficient. This linear correlation between the dynamics of non-condensables accumulation and the heat loss coefficient is also clearly shown in Fig. 9. The dynamics of the non-condensables mass increase in certain segments is practically the same in both cases, only the time axis is different due to different values of the applied overall heat transfer coefficients. As expected, the accumulation first starts in top segments 13 and 11 (Fig. 1) and latter on continues in horizontal segment 9. The non-condensables accumulation in the vertical segment 7 (Fig. 1) takes place slowly during the last 40% of the transient (after 18,000 s) in case with the lower heat transfer coefficient of 4 W m^{-2} K^{-1}. In case with the higher heat loss rate the accumulation in segment 7 starts at 3200 s, therefore, it takes place only during the last 20% of the transient duration. According to Fig. 9 the ratio of the total accumulated masses of oxygen and hydrogen is 8 along the whole transient. This is also experimentally observed in [2] and this ratio is the result of the oxygen (O_2) and hydrogen (H_2) molar ratio 1:2 (which results from the radiolysis of H_2O molecule) and their molar masses (detailed explanation of this mass ratio is presented in [8]). Fig. 9 also shows a slight decrease of the rate of accumulation of the total oxygen and hydrogen mass in the latter period of the transient in both calculations. It is caused by the decrease of the heat loss rate to the surrounding due to the decrease of the difference

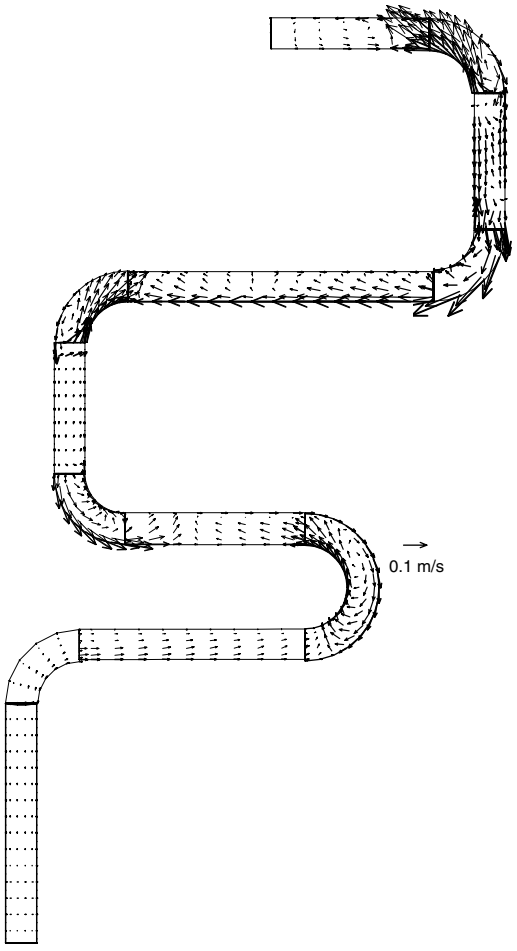

Fig. 10. Gas mixture velocity field after 8 h (overall heat transfer coefficient is 4 W m^{-2} K^{-1}).

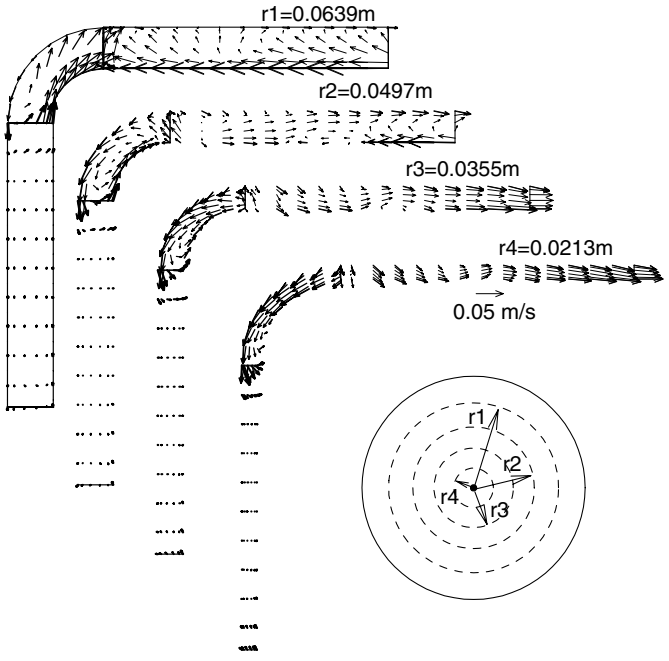

Fig. 11. Gas mixture velocity field in the vicinity of the concentration front after 8 h (overall heat transfer coefficient is 4 W m^{-2} K^{-1}).

between gas mixture and ambient temperature (the relation given with Eq. (26)).

The gas mixture velocity field is shown in Fig. 10. The complex flow structure is shown, with circulating flows in elbows and straight pipes induced by concentration differences and related buoyancy forces. The velocity field in the vertical segment 7, in the adjacent elbow 8 and horizontal segment 9 (Fig. 1) are shown in Fig. 11. The concentration front is located at the upper end of the vertical pipe, as indicated in Figs. 6 and 7. The gas mixture flow in the vertical segment below the concentration front in vertical pipe (segment number 7) is slowed. The rate of the gas mixture upward flow towards the concentration front is determined by the rate of steam condensation above the front and up to the pipeline closed top end. In the horizontal pipeline segment number 9 the gas mixture circulates due to the buoyancy forces induced by the concentration and density differences. The higher density fluid flows from right to left across the bottom wall of the horizontal segment, while reverse flow is observed in the core of the pipe and in the upper part.

Here presented gas mixture velocity fields are in the laminar range (for instance, the velocity field in the vertical segment 7 in Fig. 11) or in the transitional laminar–turbulent range (as in the elbow—segment 8 or the horizontal segment 9 in Fig. 11). According to Fig. 11 the gas mixture velocity in the vertical segment 7, below the concentration front, is lower than 0.01 m s^{-1}, and for the calculated corresponding gas mixture kinematic viscosity of 0.9×10^{-6} m^2 s^{-1} and pipe diameter 0.142 m the gas mixture Reynolds number is lower than 1600, which indicates laminar flow. For the flow domain above the concentration front, the elbow and horizontal pipe in Fig. 11, the characteristic velocity is 0.1 m s^{-1}, and the corresponding value of Reynolds number 16,000 indicates low Reynolds number turbulent flow. Hence, both laminar and turbulent flows exist in the pipeline. Regardless of this fact, the performed calculation is laminar. This implies that certain inaccuracy of the calculated velocity field could exists in some parts of the pipeline due to the performed laminar calculation; but, from the engineering point of view, the transport of the radiolytic gases in the mixture with steam governed by the condensation rate is of the prime importance (such as accumulated masses shown in Fig. 9, or acceptable agreements between calculated and measured locations of the concentration fronts shown in Figs. 6 and 8 even for different heat loss fluxes and condensation rates). Thus, details about the velocity field in areas far from the concentration front are not of the prime importance. The weak influence of the turbulent effects on the non-condensables accumulation is also demonstrated by comparing results in Figs. 6 and 8 and with Fig. 9. The results in Fig. 8 are obtained with approximately eight times higher overall heat loss coefficient and thus higher steam–non-condensables velocities and more exaggerated turbulent effects. But, nevertheless the prediction of the amounts of accumulated

non-condensable radiolytic gases practically do not differ between two cases in Fig. 9, neither the predictions of the non-condensables concentration fronts differ significantly in Figs. 6 and 8. An inclusion of a turbulent model in the calculation (such as a variant of the low-Reynolds number k–ε model) would require finer numerical grid and it would substantially prolong the calculation time (already the performed laminar calculation with the overall heat transfer coefficient of 4 W m^{-2} K^{-1} lasts about two weeks on the ordinary PC computer with 2.8 GHz processor). In non-vented pipes of small diameters the steam–gas mixture velocities are low and the flow is characterized with the Reynolds number lower than the critical one [6–8]. Therefore, the application of the turbulent model was not considered to be important and rational in most cases of practical engineering interest.

The velocity field of the wall condensate film and film thickness are shown respectively in Figs. 12 and 13. The velocity in the pipeline's vertical segments and elbows is higher than in the horizontal sections, because the liquid film thickness at the bottom of the horizontal sections is several times higher than in the vertical sections, and thus, the condensate velocity is slowed down. The condensate volume fraction along the pipeline is shown in Fig. 14. As expected, the highest condensate content is in the horizontal segments 3, 5, 9 and 13. The hydrodynamic character of the liquid film flow is determined by the Reynolds number calculated with Eqs. (9) and (10). According to the results in Figs. 12 and 13, the maximum liquid film Reynolds number (the maximum of velocity and thickness product in Eq. (9)) is estimated for the pipeline's elbows and vertical segments. According to Fig. 12 maximum liquid film velocity is 0.2 m s^{-1}, in Fig. 13 the maximum liquid film thickness in the elbow is 10^{-4} m, and for the liquid film kinematic viscosity of 0.13×10^{-6} m s^{-2} the maximum Reynolds number is 615. This value of Reynolds number indicates the wavy liquid film flow, while the transition to turbulent flow for liquid film flow on a vertical surface occurs at Reynolds numbers in the range 1600–2000 [14,16,21]. It can be also argued that the wavy liquid film on the curved surfaces of inner elbows walls and corresponding turn off points lead to the condensate droplets formation and fall. The wavy liquid film flow and the increase of the gas–condensate interface surface by droplets formation intensify the mass transfer at the film surface [21]. This conclusion contributes to the modelling

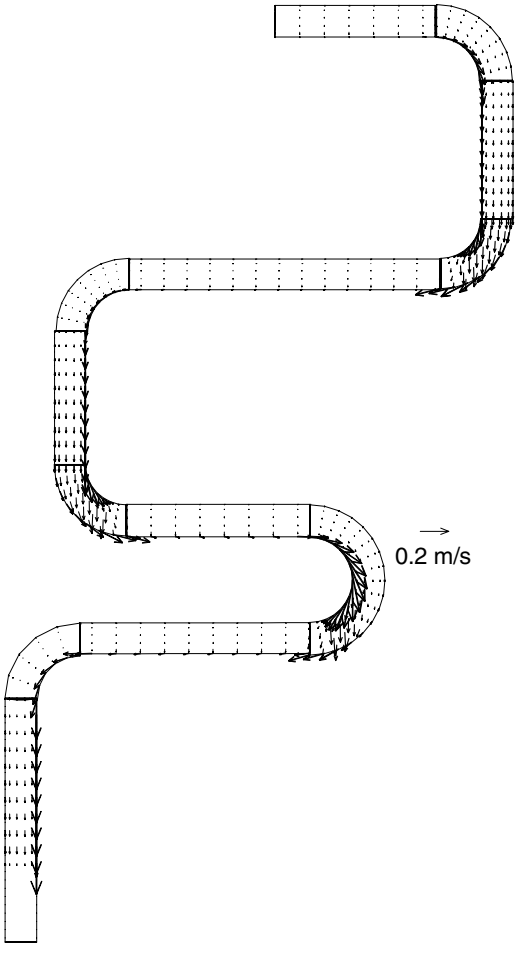

Fig. 12. Condensate velocity vectors after 8 h (overall heat transfer coefficient is 4 W m^{-2} K^{-1}).

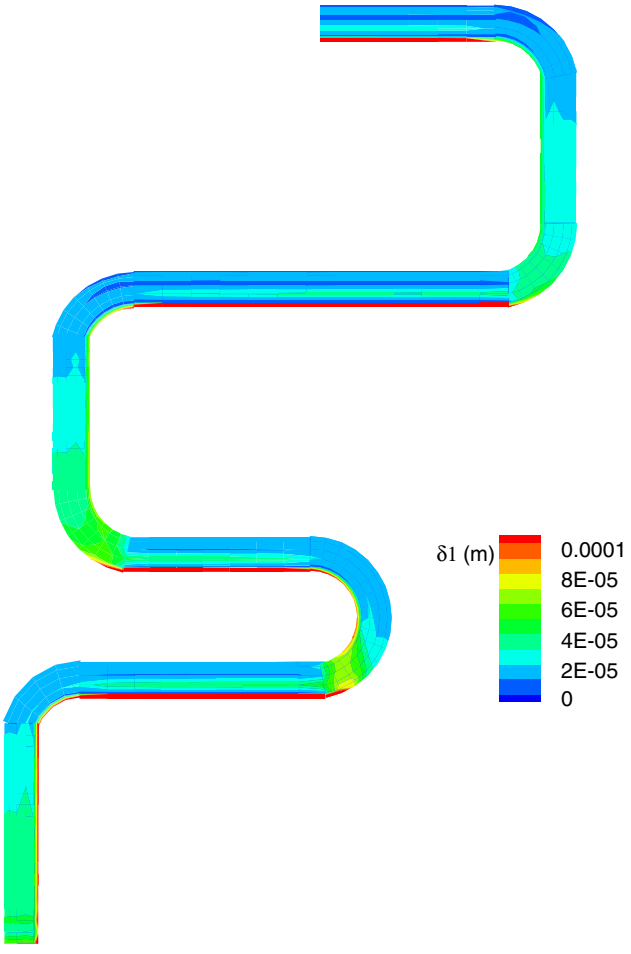

Fig. 13. Wall liquid film thickness along the pipeline after 8 h of accumulation (overall heat transfer coefficient is 4 W m^{-2} K^{-1}).

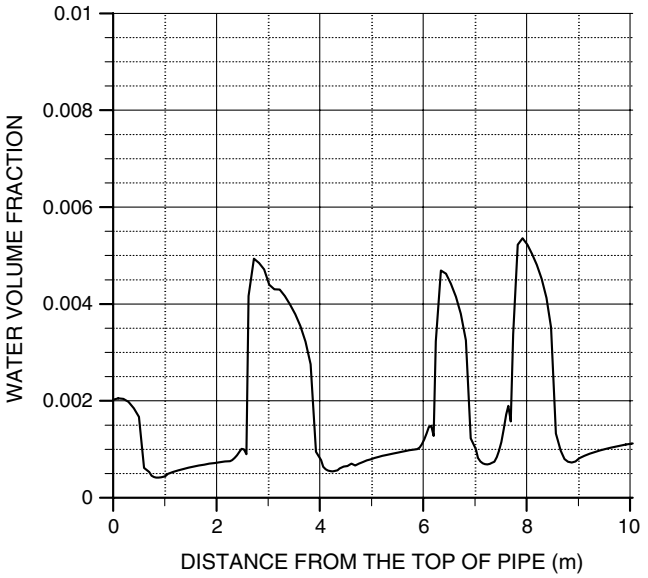

Fig. 14. Condensate volume fraction along the pipeline after 8 h of accumulation (overall heat transfer coefficient is 4 $W m^{-2} K^{-1}$).

assumption introduced in Section 3 that the liquid film is saturated with the non-condensables according to the equilibrium conditions determined with the Henry's law. Also, it could be argued that wavy liquid flow, droplets sliding on the walls and fall in the elbows do not influence substantially to the condensate drainage velocity from the pipe or condensate volume fraction in certain segments.

6. Conclusion

The results of the development of the physical and mathematical models and corresponding numerical code HELIO are presented for the simulation and analyses of radiolytic gases accumulation in non-vented steam pipelines. The developed model consists of the mass, momentum and energy conservation equations for the mixture of steam and non-condensable gases and liquid film flow, as well as of the mass conservation equations for non-condensable gases. The necessary thermal-hydraulic and physicochemical relations for the prediction of mass, momentum and energy transfers at the gas mixture and liquid film interface are stated, together with the governing equations for the calculation of heat losses and steam condensation.

The three-dimensional simulations of the radiolytical gases accumulation in the complex pipeline of the Residual Heat Removal System in the Hamaoka NPP have been performed. The results show complete thermal-hydraulic conditions in the pipeline, consisting of gas mixture and condensate velocity fields, temperature field, and condensate void fraction. The propagation of the concentration front of the radiolytic gases along the pipeline is predicted. The acceptable agreement between experimentally measured and calculated temperatures of the steam–non-condensables gas mixture along the pipeline is obtained. Presented results show that the HELIO code can be used for the simulation and analyses of the radiolytic gases accumulation in non-vented pipelines. Its results are a support to the analyses of incident conditions, and they indicate a possibility, amount and time periods of the radiolytic gases accumulation in pipelines of various configurations. The HELIO code can be applied for the optimization of locations of necessary temperature measurements within the plant for the purpose of radiolytic gases accumulation detection, which would reduces the operational and maintenance costs.

The presented modelling approach is consistent and robust regarding the simultaneous three-dimensional solution of the heat and mass transfer in the system consisting of the steam–non-condensable gases mixture and the thin liquid film on the pipe's wall. It provides reliable results about non-condensables accumulation rates in non-vented single pipes and complex pipelines for simulation times ranging from several to tens of hours. Despite complexity and simplified modelling approaches to some processes and effects, mainly regarding the thin liquid film wavy flow, gas–liquid interface mass and momentum transport or low Reynolds number turbulent flows in certain parts of the pipeline, the HELIO code model is based on the first principles and no fitting parameters are applied. Further investigation of this phenomenon could be directed towards some specific effects and model constituents, such as transport properties of ternary gas mixtures, stability of very thin liquid films on curved surfaces, dropwise condensation in the presence of non-condensables, sessile drops formation, etc.

References

[1] V. Gerasimov, A. Monakhov, Nuclear Engineering Materials, first ed., Mir, Moscow, 1983, pp. 98, 167–170.
[2] T. Narabayashi, Y. Yamamoto, T. Yamamoto, N. Ichikawa, A. Sudo, R. Matsukawa, Study on thermal-hydraulic accumulation mechanisms of non-condensable gases, in: JSME/ASME Proceedings of the Eleventh International Conference on Nuclear Engineering, Tokyo, Japan, 2003, paper ICONE11-36510.
[3] U. Stoll, Hydrogen accumulation/combustion; lessons learned in various countries, example of Brunsbuettel in Germany, Invited Lecture, in: The Eleventh International Conference on Nuclear Engineering, Tokyo, Japan, 2003.
[4] U. Kleen, U., Hartel, W., Rupture of vessel head spray line at brunbuettel nuclear power station—root cause analysis and measures for preventing radiolysis gas reactions in the future, invited lecture, in: The Eleventh International Conference on Nuclear Engineering, Tokyo, Japan, 2003.
[5] T. Diesselhorst, Accumulation of radiolytic gases in BWR steam piping and components, in: JSME/ASME Proceedings of the Eleventh International Conference on Nuclear Engineering, Tokyo, Japan, 2003, paper ICONE11-36558.
[6] V. Stevanovic, Z. Stosic, U. Stoll, HELIO code simulation of condensation induced hydrogen accumulation in slightly inclined non-vented pipe, in: ASME Proceedings of the Twelfth International Conference on Nuclear Engineering, Washington DC, 2004, paper ICONE12-49534.
[7] V. Stevanovic, Z. Stosic, U. Stoll, Condensation induced hydrogen accumulation in a non-vented pipe, in: JSME/ASME, Proceedings of

the Eleventh International Conference on Nuclear Engineering, Tokyo, Japan, 2003, paper ICONE11-36384.
[8] V. Stevanovic, Z. Stosic, U. Stoll, Condensation induced non-condensables accumulation in a non-vented vertical pipe, Int. J. Heat Mass Transfer 48 (2005) 83–103.
[9] S.V. Patankar, Numerical Heat Transfer and Fluid Flow, first ed., Hemisphere, New York, 1980.
[10] Z. Stosic, V. Stevanovic, Advanced three-dimensional two-fluid porous media method for transient two-phase flow thermal-hydraulics in complex geometries, Numer. Heat Transfer, Part B: Fundam. 41 (2002) 263–289.
[11] T. Diesselhorst, V. Stevanovic, Detailed investigation of radiolytic gas accumulation in BWR piping with the CMFD-code HELIO, in: Proceedings of the 11th International Topical Meeting on Nuclear Reactor Thermal-Hydraulics—NURETH-11, Avignon, France, 2005, paper 305.
[12] J.U. Brackbill, D.B. Kothe, C. Zemach, A continuum method for modelling surface tension, J. Comput. Phys. 100 (1992) 335–354.
[13] J.P. Holman, Heat Transfer, ninth ed., McGraw-Hill, New York, 1990, pp. 601–602.
[14] A. Bejan, Heat Transfer, first ed., Wiley, New York, 1993, pp. 398–405, 588, 592.
[15] X. Ji, J. Yan, Saturated thermodynamic properties for the air–water system at elevated temperatures and pressures, Chem. Eng. Sci. 58 (2003) 5069–5077.
[16] V.P. Isachenko, V.A. Osipova, A.S. Sukomel, Heat Transfer, third ed., Mir, Moscow, 1980, pp. 278–279.
[17] E. Schmidt, Properties of Water and Steam in SI-Units, first ed., Springer-Verlag, Berlin, 1969.
[18] R.C. Reid, J.M. Prausnitz, B.E. Poling, The Properties of Gases and Liquids, fourth ed., McGraw-Hill, New York, 1987 (Chapter 11).
[19] R.B. Bird, W.E. Stewart, E.N. Lightfoot, Transport Phenomena, second ed., John Wiley & Sons, Inc., New York, 2002, pp. 27, 276.
[20] D.B. Spalding, Developments in the IPSA procedure for numerical computation of multiphase-flow phenomena with interphase slip, unequal temperatures, etc., in: T.M. Shin (Ed.), Numerical Properties and Methodologies in Heat Transfer, Hemisphere Publ. Co., 1983, pp. 421–436.
[21] C. Boyadjiev, V. Beschkov, Mass Transfer in Liquid Film Flows, Mir, Moskva, 1988, pp. 12–14, 116.